The Astrophysical Journal Letters, 926:L7 (12pp), 2022 February 20 https://doi.org/10.3847/2041-8213/ac4da0

NEID Rossiter–McLaughlin Measurement of TOI-1268b: A Young Warm Saturn Aligned with Its Cool Host Star

Jiayin Dong[1,2], Chelsea X. Huang[3,4], George Zhou[3], Rebekah I. Dawson[1,2,5,6], Gumundur K. Stefánsson[7,43], Chad F. Bender[8], Cullen H. Blake[9], Eric B. Ford[1,2,5,6], Samuel Halverson[4,10,44], Shubham Kanodia[1,2,11], Suvrath Mahadevan[1,2,45], Michael W. McElwain[12], Joe P. Ninan[1,2], Paul Robertson[13,46], Arpita Roy[14,15], Christian Schwab[16], Daniel J. Stevens[1,2], Ryan C. Terrien[17], Andrew Vanderburg[4], Adam L. Kraus[18], Stephanie Douglas[19], Elisabeth Newton[20], Rayna Rampalli[20], Daniel M. Krolikowski[18], Karen A. Collins[21], Joseph E. Rodriguez[22], Dax L. Feliz[23], Gregor Srdoc[24], Carl Ziegler[25], Khalid Barkaoui[26,27], Francisco J. Pozuelos[26,28], Emmanuel Jehin[28], C. Michaël[26], Zouhair Benkhaldoun[29], Pablo Lewin[30], Raquel Forés-Toribio[31,32], Jose A. Muñoz[31,32], Kim K. McLeod[33], Fiona Powers Özyurt[33], Ferran Grau Horta[34], Felipe Murgas[35,36], David W. Latham[21], Samuel N. Quinn[21], Allyson Bieryla[21], Steve B. Howell[37], Crystal L. Gnilka[37,38], David R. Ciardi[38], Michael B. Lund[38], Courtney D. Dressing[39], Steven Giacalone[39], Arjun B. Savel[40], Ivan A. Strakhov[41], Alexander A. Belinski[41], George R. Ricker[4], S. Seager[4,27,42], Joshua N. Winn[7], Jon M. Jenkins[37], Guillermo Torres[21], and Martin Paegert[21]

[1] Department of Astronomy & Astrophysics, 525 Davey Laboratory, The Pennsylvania State University, University Park, PA 16802, USA; jdong@psu.edu
[2] Center for Exoplanets and Habitable Worlds, 525 Davey Laboratory, The Pennsylvania State University, University Park, PA 16802, USA
[3] University of Southern Queensland, Centre for Astrophysics, West Street, Toowoomba, QLD 4350, Australia
[4] Department of Physics and Kavli Institute for Astrophysics and Space Research, Massachusetts Institute of Technology, Cambridge, MA 02139, USA
[5] Institute for Computational and Data Sciences, The Pennsylvania State University, University Park, PA 16802, USA
[6] Center for Astrostatistics, 525 Davey Laboratory, The Pennsylvania State University, University Park, PA 16802, USA
[7] Department of Astrophysical Sciences, Princeton University, 4 Ivy Lane, Princeton, NJ 08540, USA
[8] Steward Observatory, The University of Arizona, 933 N. Cherry Avenue, Tucson, AZ 85721, USA
[9] Department of Physics and Astronomy, University of Pennsylvania, 209 S 33rd Street, Philadelphia, PA 19104, USA
[10] Jet Propulsion Laboratory, California Institute of Technology, 4800 Oak Grove Drive, Pasadena, CA 91109, USA
[11] Penn State Extraterrestrial Intelligence Center, 525 Davey Laboratory, The Pennsylvania State University, University Park, PA, 16802, USA
[12] Exoplanets and Stellar Astrophysics Laboratory, NASA Goddard Space Flight Center, Greenbelt, MD 20771, USA
[13] Department of Physics & Astronomy, University of California, Irvine, CA 92697, USA
[14] Space Telescope Science Institute, 3700 San Martin Drive, Baltimore, MD 21218, USA
[15] Department of Physics and Astronomy, Johns Hopkins University, 3400 N Charles Street, Baltimore, MD 21218, USA
[16] Department of Physics and Astronomy, Macquarie University, Balaclava Road, North Ryde, NSW 2109, Australia
[17] Carleton College, One North College Street, Northfield, MN 55057, USA
[18] Department of Astronomy, The University of Texas at Austin, Austin, TX 78712, USA
[19] Department of Physics, Lafayette College, 730 High Street, Easton, PA 18042, USA
[20] Department of Physics and Astronomy, Dartmouth College, Hanover, NH 03755, USA
[21] Center for Astrophysics |Harvard & Smithsonian, 60 Garden Street, Cambridge, MA 02138, USA
[22] Department of Physics and Astronomy, Michigan State University, East Lansing, MI 48824, USA
[23] Department of Physics and Astronomy, Vanderbilt University, Nashville, TN 37235, USA
[24] Kotizarovci Observatory, Sarsoni 90, 51216 Viskovo, Croatia
[25] Department of Physics, Engineering and Astronomy, Stephen F. Austin State University, 1936 North Street, Nacogdoches, TX 75962, USA
[26] Astrobiology Research Unit, Université de Liège, 19C Allée du 6 Août, B-4000 Liège, Belgium
[27] Department of Earth, Atmospheric, and Planetary Sciences, Massachusetts Institute of Technology, Cambridge, MA 02139, USA
[28] Space sciences, Technologies and Astrophysics Research (STAR) Institute, Université de Liège, Belgium
[29] Oukaimeden Observatory, High Energy Physics and Astrophysics Laboratory, Cadi Ayyad University, Marrakech, Morocco
[30] The Maury Lewin Astronomical Observatory, Glendora, CA 91741, USA
[31] Departamento de Astronomía y Astrofísica, Universidad de Valencia, E-46100 Burjassot, Valencia, Spain
[32] Observatorio Astronómico, Universidad de Valencia, E-46980 Paterna, Valencia, Spain
[33] Department of Astronomy, Wellesley College, Wellesley, MA 02481, USA
[34] Observatori de Ca l'Ou, Carrer de dalt 18, E-08282 Sant Martí Sesgueioles, Barcelona, Spain
[35] Instituto de Astrofísica de Canarias (IAC), E-38205 La Laguna, Tenerife, Spain
[36] Departamento de Astrofísica, Universidad de La Laguna (ULL), E-38206 La Laguna, Tenerife, Spain
[37] NASA Ames Research Center, Moffett Field, CA 94035, USA
[38] NASA Exoplanet Science Institute, Caltech/IPAC, Mail Code 100-22, 1200 E. California Boulevard, Pasadena, CA 91125, USA
[39] Department of Astronomy, University of California, Berkeley, CA, USA
[40] Department of Astronomy, University of Maryland, College Park, MD, USA
[41] Sternberg Astronomical Institute, M.V. Lomonosov Moscow State University, 13, Universitetskij pr., 119234, Moscow, Russia
[42] Department of Aeronautics and Astronautics, Massachusetts Institute of Technology, Cambridge, MA 02139, USA
Received 2021 December 10; revised 2022 January 19; accepted 2022 January 20; published 2022 February 16

[43] Henry Norris Russell Fellow.
[44] Sagan Fellow.
[45] NEID Principal Investigator.
[46] NEID Instrument Team Project Scientist.

Abstract

Close-in gas giants present a surprising range of stellar obliquity, the angle between a planet's orbital axis and its host star's spin axis. It is unclear whether the obliquities reflect the planets' dynamical history (e.g., aligned for in situ formation or disk migration versus misaligned for high-eccentricity tidal migration) or whether other mechanisms (e.g., primordial misalignment or planet–star interactions) are more important in sculpting the obliquity distribution. Here we present the stellar obliquity measurement of TOI-1268 (TIC-142394656, $V_{\rm mag} \sim 10.9$), a young K-type dwarf hosting an 8.2 day period, Saturn-sized planet. TOI-1268's lithium abundance and rotation period suggest the system age between the ages of the Pleiades cluster (∼120 Myr) and the Prasepe cluster (∼670 Myr). Using the newly commissioned NEID spectrograph, we constrain the stellar obliquity of TOI-1268 via the Rossiter–McLaughlin effect from both radial velocity and Doppler tomography signals. The 3σ upper bounds of the projected stellar obliquity $|\lambda|$ from both models are below 60°. The large host star separation ($a/R_\star \sim 17$), combined with the system's young age, makes it unlikely that the planet has realigned its host star. The stellar obliquity measurement of TOI-1268 probes the architecture of a young gas giant beyond the reach of tidal realignment ($a/R_\star \gtrsim 10$) and reveals an aligned or slightly misaligned system.

Unified Astronomy Thesaurus concepts: Extrasolar gaseous giant planets (509); Radial velocity (1332); Transit photometry (1709); Stellar activity (1580); Exoplanet dynamics (490)

1. Introduction

Stellar obliquity describes the angle between a planet's orbital axis and its host star's spin axis. Giant planets orbiting close to their host stars present a surprisingly wide range of stellar obliquity from 0° to 180° (e.g., Albrecht et al. 2012). It is still unclear whether the stellar obliquities reflect close-in giant planets' origin channels—aligned for in situ formation or disk migration versus misaligned for high-eccentricity tidal migration (see Section 3.2 of Dawson & Johnson 2018 for a review)—or whether other mechanisms are more important in sculpting the obliquity distribution. Proposed physical processes include the planet's primordial misalignment of the protoplanetary disk (e.g., Batygin 2012), the star's magnetospheric interactions with the protoplanetary disk (e.g., Lai et al. 2011), and angular momentum transport to the stellar surface by stellar internal gravity waves (e.g., Rogers et al. 2012, 2013). Moreover, close-in giant planets originating from coplanar high-eccentricity tidal migration (Petrovich 2015) may be aligned. In addition to these proposed mechanisms, planet–star tidal interactions may have altered the obliquity distribution for hot-Jupiter hosts (e.g., Winn et al. 2010). Consequently, measuring the obliquities of warm Jupiters—orbiting too far from their star to cause tidal realignment ($a/R_\star \gtrsim 10$)—could be essential to disentangle these proposed mechanisms.

The Transiting Exoplanet Survey Satellite (TESS; Ricker et al. 2015) discovered a large sample of warm Jupiters around bright stars that are feasible for stellar obliquity measurements using the Rossiter–McLaughlin (RM) effect (McLaughlin 1924; Rossiter 1924). As a planet transits across its host star, it modifies the shape of spectral lines of the star that can be used to infer its positions on the stellar disk relative to the stellar spin axis, and constrain the projected stellar obliquity. Here we use the newly commissioned NEID spectrograph (Schwab et al. 2016) on the 3.5 m WIYN telescope to conduct the RM-effect measurement of TOI-1268 (TIC-142394656, $V_{\rm mag} \sim 10.9$), the host of a 8.2 day, Saturn-sized planet. The large host star separation (i.e., large $a/R_\star$) of TOI-1268b, combined with the system's young age, makes it unlikely that the planet has realigned its host star. The stellar obliquity measurement of TOI-1268 probes the architecture of a young, warm giant system beyond the reach of tidal realignment.

In Section 2, we present the photometric, high-resolution imaging, and spectroscopic observations of TOI-1268 using Transiting Exoplanet Survey Satellite (TESS), Kilodegree Extremely Little Telescope (KELT), `Alopeke, PHARO, Tillinghast Reflector Echelle Spectrograph (TRES), and NEID. In Section 3, we model the stellar parameters and estimate the system's age using the stellar rotation period and lithium abundance. In Section 4, we model the planetary parameters from the TESS and ground-based transit light curves (Section 4.1) and measure the stellar obliquity of TOI-1268 using the RM effect and Doppler tomography (DT; Section 4.2). Finally, in Section 5, we discuss the implication of the stellar obliquity of TOI-1268 and place the target in the context of exoplanetary systems.

2. Observations

2.1. TESS Photometry

The TESS data for TOI-1268 are available as 10×10 subimages with 2 minute time sampling, and as part of full-frame images (FFIs) with 30 minute sampling. We obtained three sectors of TESS Primary Mission data from 2019 August 15 to 2019 September 11 (Sector 15) and from 2020 January 21 to 2020 March 18 (Sectors 21 and 22), and one sector of TESS extended mission data from 2021 July 23 to 2021 August 20 (Sector 41). The target will have at least two more sectors of TESS observations in Sector 48 (2022 January 28 to 2022 February 26) and Sector 49 (2022 February 26 to 2022 March 26).

The transit signal was detected with a period of ∼8.16 days at high significance independently by the NASA Science Processing Operations Center (SPOC) pipeline (Jenkins et al. 2016) and the MIT Quick-Look Pipeline (QLP; Huang et al. 2020a, 2020b), and was released to the public for follow-up observations as TOI-1268.01. In total, 14 transits of TOI-1268b were observed by TESS. The TESS light curves do not show any strong instrument systematics. We used the Pre-search Data Conditioning SAP flux (`PDC_SAPFLUX`; Stumpe et al. 2012, 2014) for the light-curve analysis.

2.2. Ground-based Transit Photometry

Through the TESS Follow-up Observing Program (TFOP) collaboration (Collins et al. 2018), we observed eight full or partial transits of TOI-1268b with ground-based seeing-limited telescopes, including three transits observed simultaneously with the TESS observations. We used the `TESS`

`Transit Finder`, which is a customized version of the `Tapir` software package (Jensen 2013), to schedule our transit observations. These observations confirm that the transiting signal originated from within less than 6″ of the target star. Gaia EDR3 (Lindegren et al. 2021) reports no additional stars within 10″ of TOI-1268.

We include two good-quality full transits that were taken simultaneously with TESS in our transit modeling (see Figure 1). The first transit was taken on UT 2020 January 26 by the Deep Sky West 0.5 m telescope near Rowe, NM, USA, in the g' band and detected an on-time transit in a 10.″9 aperture. The second transit was taken on UT 2020 February 3 simultaneously in g_p and z_s filters with a 6.″3 aperture from the Las Cumbres Observatory Global Telescope (LCOGT; Brown et al. 2013) 0.4 m network node at Haleakala Observatory. The light curves were reduced with `AstroImageJ` (Collins et al. 2017).

In addition, we obtained six transits of TOI-1268b with full or partial transit baselines from various ground-based facilities. These transit observations played an important role in confirming the transit to be on target and ruling out nearby eclipsing binaries. We do not include these observations in our transit model because of their partial transit baselines or additional complications due to meridian flip (i.e., telescope pointing crossing the meridian during the observation) that introduces systematic flux offset. We list the observations below and these data can be found on the ExoFOP website.[47]

1. On UT 2020 January 9, an ingress was observed to be on target from the Kotizarovci Observatory 0.3 m Telescope, near Viskovo, Croatia, in a Baader R 610 nm longpass filter using a 10.″8 aperture, marginally contaminated by a nearby star.
2. On UT 2020 January 10, an egress was observed from the LCOGT 0.4 m telescope from Teide Observatory in the z_s filter using an uncontaminated 10.″2 aperture.
3. On UT 2020 March 6, the TRAPPIST-North team observed an on-time, almost full transit in the B band. The detection is complicated by a meridian flip at ingress and a strong increase in sky background as the nominal time of egress approached.
4. On UT 2021 April 18, a partial transit was observed in the B band from the OAUV-TURIA1 (0.143 m) telescope near Valencia, Spain. The detection is complicated by a meridian flip during predicted ingress and strong residuals.
5. Also on UT 2021 April 18, the same transit was observed in a 6.″7 uncontaminated aperture in the B band from the Observatory de Ca l'Ou 0.4 m telescope near Barcelona, Spain.
6. On UT 2021 April 27, a partial was observed in the g band using an uncontaminated 4.″7 aperture from the Wellesley College Whitin Observatory CDK700 telescope near Wellesley, MA, USA.

2.3. Long-term Photometric Observation

The KELT Survey (Pepper et al. 2003, 2007) also monitored the star for over two years from BJD 2,455,976 to BJD 2,457,022 as part of its normal survey. The precision of the KELT photometry is not sufficient to detect the transit signals. However, the long-term monitoring from KELT was used to measure the stellar rotation period. The Lomb–Scargle periodogram (Lomb 1976; Scargle 1982; VanderPlas 2018) of the KELT light curve reveals that the star has a rotation period of 10.8 days (Figure 2). This detection helps to break the degeneracy between the rotation period determined from the TESS light curves, which shows two peaks at ∼5 days and ∼10 days.

2.4. High-resolution Imaging Observation

High-resolution imaging is required to detect nearby companions or background objects that cannot be resolved by seeing-limited photometry. We obtained both adaptive optics (AO) and speckle imaging of TOI-1268, as shown in Figure 3. On UT 2020 January 8, the PHARO instrument (Hayward et al. 2001) on Palomar 5 m collected AO images of TOI-1268 in the narrowband $Br\gamma$ filter. No companions are identified down to a contrast of 5.481 magnitudes at 0.″5. On UT 2021 February 2, the `Alopeke speckle instrument (Scott 2019) on Gemini North 8 m took simultaneous speckle imaging in the 832 and 562 nm bands. No companions are detected down to a contrast of 6.36 mag at 0.″5.

Although not shown in Figure 3, we obtained the following observations on the Sternberg Astronomical Institute (SAI) 2.5 m telescope located at Mt Shatdzhatmaz in the North Caucasus and on the Shane 3 m telescope at Lick Observatory in Mount Hamilton, CA, USA. On UT 2020 November 29, the Speckle Polarimeter on SAI 2.5 m obtained speckle imaging of TOI-1268 in I filter. On UT 2019 November 12, the ShARCS instrument (Kupke et al. 2012; Gavel et al. 2014) on Shane 3 m collected AO images of TOI-1268 in the Ks and J filters. The ShARCS data were reduced and analyzed using the open-source Python-based SImMER pipeline available on GitHub and described in previous publications (Hirsch et al. 2019; Savel et al. 2020). TOI-1268 appeared single in both observations.

2.5. Long-term Spectroscopic Observation

We obtained 14 spectra with TRES on the 1.5 m telescope at the Fred Lawrence Whipple Observatory, from UT 2019 December 10 to UT 2020 December 27. TRES has a resolving power of $R \approx 44{,}000$, and covers a wavelength range from 385 to 906 nm. The spectra were extracted following Buchhave et al. (2010), and radial velocities were measured using a cross-correlation analysis against a template spectrum generated from a median combination of all TRES observed spectra (Quinn et al. 2012). We also make use of the TRES spectra to measure the atmospheric parameters of the host star via the Stellar Classifications Pipeline (SPC; Buchhave et al. 2012, 2014), finding an effective temperature of $T_{\rm eff} = 5288 \pm 50$ K, surface gravity $\log g$ of 4.62 ± 0.10, and bulk metallicity [M/H] of $+0.16 \pm 0.08$. The projected broadening width $v_{\rm broadening} = 4.1 \pm 0.5$ km s^{-1}. The $v_{\rm broadening}$ here does not correct for macroturbulence, so the stellar rotational velocity $v \sin i_\star$ must be smaller than the reported value.

TOI-1268 exhibits significant photometric variability due to its youth, and as such we also expect significant jitter in the radial velocities (RVs). The TRES RVs exhibit scatter at the 50 m s^{-1} level with a typical RV precision at ∼30 m s^{-1}. The Lomb–Scargle periodogram of the TRES RVs detects neither the stellar rotation period nor the planetary orbital period due to

[47] https://exofop.ipac.caltech.edu/tess/

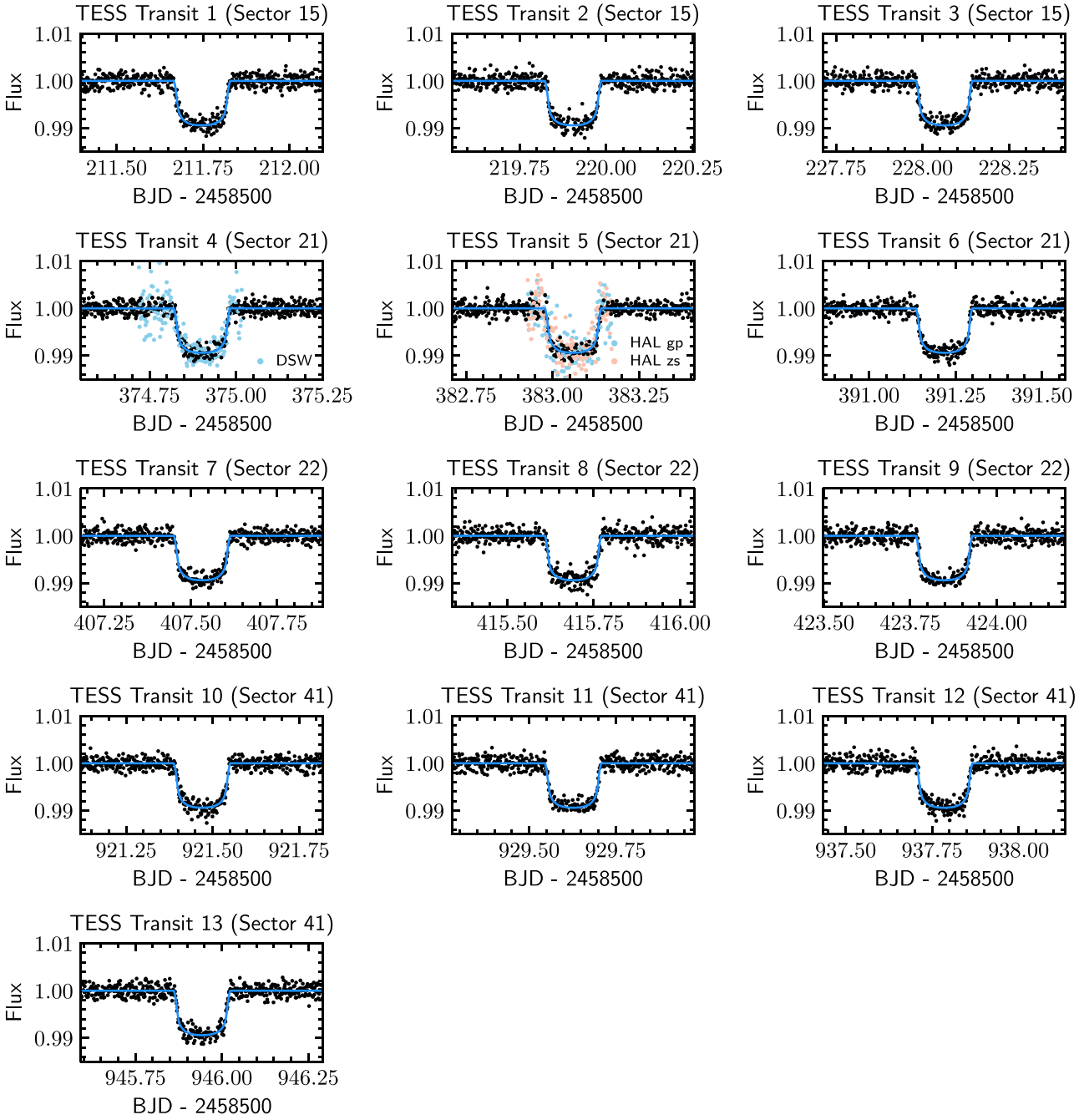

Figure 1. Detrended TESS and ground-based transit light curves of TOI-1268b. In total we obtained 13 TESS transits in 2 minute cadence from Sectors 15, 21, 22, and 41, and 8 more full or partial transits from ground-based observatories. The Deep Sky West (DSW; simultaneously with TESS Transit 4) and Haleakala (simultaneously with TESS Transit 5) observations are jointly fitted with the TESS transits. The blue curves present the best-fit transit models.

sparse observations and entangled stellar activity and planetary signals.

2.6. Transit Spectroscopic Observation

We observed one transit of TOI-1268b with the extremely high precision NEID spectrograph (Halverson et al. 2016; Schwab et al. 2016) on the 3.5 m WIYN telescope at the Kitt Peak National Observatory (KPNO) in Tucson, AZ, USA. NEID is a fiber-fed (Kanodia et al. 2018), actively environmentally stabilized spectrograph (Stefansson et al. 2016; Robertson et al. 2019) with a resolution of $R \approx 110{,}000$ and a wavelength coverage of 380 nm to 930 nm. The observation was taken on UT 2021 May 4 during the transit of TOI-1268b, and covered about 1.5 hr baseline before the transit. We used an exposure time of 8 minutes for each observation, and in total obtained 37 spectra. The spectra were extracted and radial velocities were reduced by the NEID standard data reduction pipeline `NEID-DRP v1.1.2`,[48] which derives cross-correlation-based RVs (we used `CCFRVMOD` data produced by the pipeline), and separately by the `SERVAL` pipeline (Zechmeister et al. 2018), which derives RVs using the reconstructed stellar template from observations (see Section 3.1 in Stefansson et al. 2021 for the NEID customization). The two pipelines derive

[48] https://neid.ipac.caltech.edu/docs/NEID-DRP

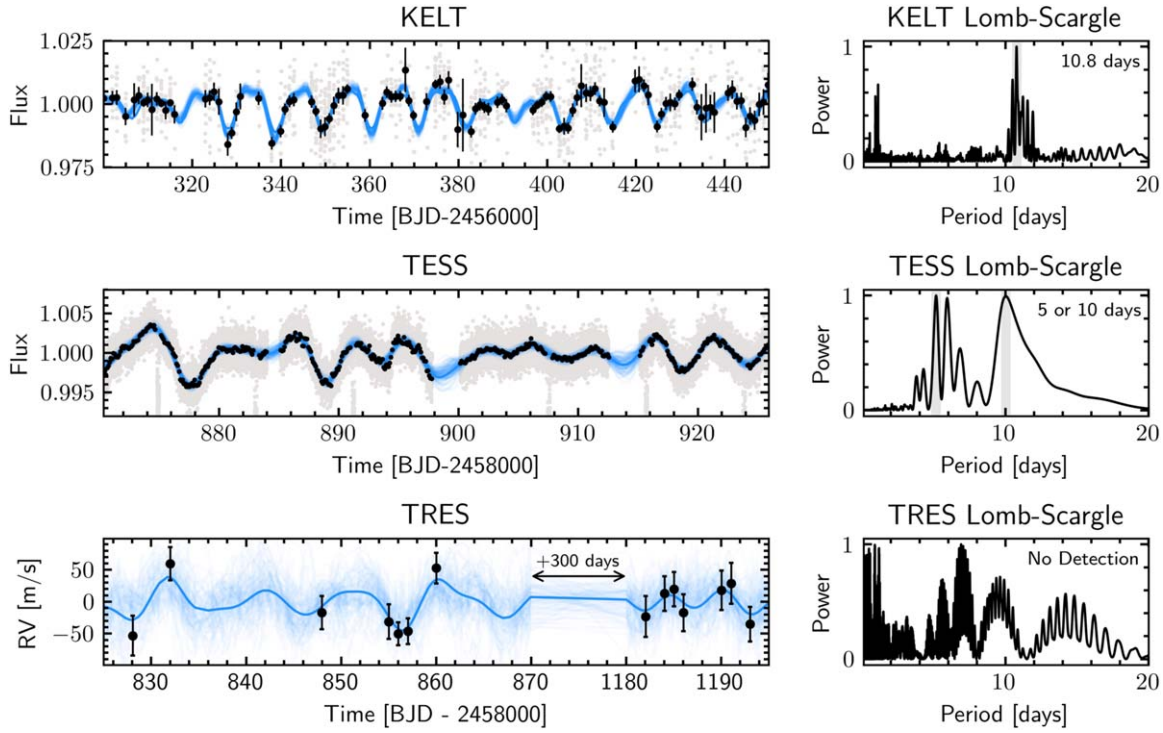

Figure 2. Long-term photometric and spectroscopic observations of TOI-1268 using KELT, TESS, and TRES. Only a fraction of the KELT and TESS light curves are presented due to the limited space. The stellar rotation period is clearly detected in KELT and TESS photometry in the Lomb–Scargle periodogram. Neither stellar rotation period nor planetary orbital period is detected in TRES data. Applying a rotational kernel in Gaussian Process (GP) on KELT, TESS, and TRES data (see Section 3), we infer the stellar rotation period as 10.84 ± 0.07 days, consistent with the periodogram results. The blue curves are predicted GP models, and the light blue curves are drawn from posteriors.

similar RVs that are consistent within 1σ uncertainties except a few data points. The achieved median, photon-limited RV precision for both pipelines is $\sim 5.8\,\mathrm{m\,s^{-1}}$. Reduced RVs are presented in Figure 5.

To directly measure the Doppler shadow cast by the planet on the spectroscopic line profiles of the star, we perform a least-squares deconvolution (Donati et al. 1997) between the NEID spectra and a synthetic nonrotating spectral template. The synthetic template is generated using a set of ATLAS-9 atmosphere models (Castelli & Kurucz 2004) at the stellar atmosphere parameters of TOI-1268. The line profiles are computed for each order of an observation, and weighted-average combined into a single line profile per epoch. Section 4.2 describes the modeling of the line profiles to retrieve the planetary orbital obliquity, and Figure 5 shows the tomographic shadow of the planetary transit.

3. Stellar Properties

3.1. SED Modeling

We use `astroARIADNE`[49] to model the spectra energy distribution (SED) of the star. We use the three Gaia band magnitudes, three 2MASS band magnitudes, and the four WISE band magnitudes in the modeling, and use the Gaia parallax, $T_{\rm eff}$, and [M/H] derived from the TRES spectra as our priors. The uncertainties of the photometry bands are inflated following methods described in `EXOFASTv2` (Eastman et al. 2013, 2019). We use the PHOENIX models and MIST isochrones in the SED modeling. The best-fitted stellar parameters and their uncertainties are $R_\star = 0.86 \pm 0.02\,R_\odot$, $M_\star = 0.9 \pm 0.13\,M_\odot$, $T_{\rm eff} = 5257 \pm 40$ K, $\log g = 4.52 \pm 0.07$, and $[\mathrm{M/H}] = +0.17 \pm 0.06$.

3.2. Stellar Rotation

As discussed in Sections 2.1 and 2.3, the star exhibits a clear rotation signature in both the TESS and KELT photometry. We use a Gaussian Process (GP) model with a rotation kernel to infer the rotation period of TOI-1268. The rotation kernel is composed of two damped harmonic oscillators with the characteristic frequencies of $1/P$ and $2/P$ to model stellar variability at the rotation period itself and at harmonics. Five free parameters in the rotation term are the rotation period P, two quality factors Q_0 and dQ describing the damping timescales of each oscillator, and σ and f describing the amplitudes of each oscillator. We apply the kernel to the KELT, TESS, and TRES observations using the `celerite2` package (Foreman-Mackey et al. 2017; Foreman-Mackey 2018). Transits are masked from TESS light curves. We run Markov Chain Monte Carlo (MCMC) to sample posteriors using the `PyMC` package (Salvatier et al. 2016). We sample four chains, each with 10,000 burn-in steps, 3000 draws, and use a target acceptance rate of 0.95. We assess the MCMC convergence using the Gelman–Rubin diagnostic ($\hat{R} < 1.01$ for convergence) and find all the inferred parameters have $\hat{R} \leqslant 1.001$. In Figure 2, we present the flux and RV variations predicted by GP models in blue curves and draw from the posteriors in light blue curves. The GP models perform well on predicting flux variations on TRES and TESS light curves, whereas perform they poorly on TRES RVs due to the sparse

[49] https://github.com/jvines/astroARIADNE

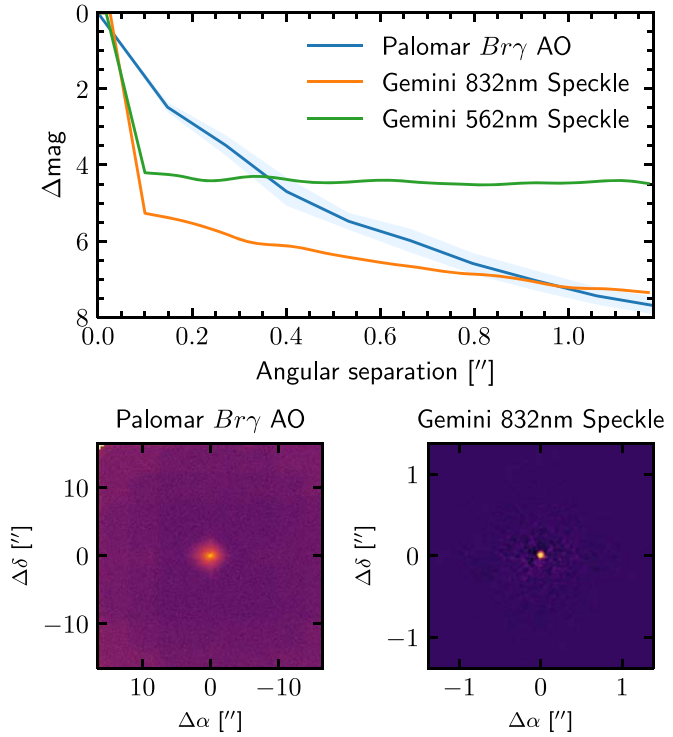

Figure 3. Upper: the 5σ contrast curves of TOI-1268 from Palomar in the $Br\gamma$ filter from adaptive optics (AO) imaging, and from Gemini North in the 832 nm and 562 nm bands from speckle imaging. Lower: the AO image (left) and reconstructed speckle image (right) of TOI-1268. No nearby companions are identified.

sampling on TRES data and complication from planetary signal. We test the GP models with and without TRES RVs and find similar rotation period posteriors. The inferred rotation period for TOI-1268 is $P_{\rm rot} = 10.84 \pm 0.07$ days. Combining the stellar rotation period and radius, the equatorial rotational velocity of TOI-1268 is $v_{\rm rot} = 2\pi R_\star / P_{\rm rot} = 4.02 \pm 0.10$ km s^{-1}.

The inclination of the star $i_\star$ can be inferred from the projected rotational velocity of the host star and its equatorial rotational velocity (Masuda & Winn 2020). Since we only know the projected broadening width ($v_{\rm broadening} = 4.1 \pm 0.5$ km s^{-1}), the true projected rotational velocity could be smaller and this difference could lead to an overestimation of the inclination. We apply priors on $P_{\rm rot}$ and $R_\star$ from stellar fits, as well as a uniform prior on $\cos i_\star$, and infer $i_\star = 76^\circ \pm 10^\circ$ using the MCMC.

3.3. Stellar Age

TOI-1268 does not belong to any known association based on a search of the BANYAN Σ catalog (Gagné et al. 2018). We used the `Comove` package[50] (Tofflemire et al. 2021) to query Gaia EDR3 (Lindegren et al. 2021) and search for associations within 50 pc, and did not find any clear clustering in velocity space. We identified 95 candidate stars that are brighter than TESS magnitude of 13.5, and could be associated with TOI-1268, and use the Discrete Fourier Transform (DFT) clean algorithm in `VARTOOLS` (Hartman & Bakos 2016) to measure their rotation periods with TESS FFI light curves. The relation between the rotation period and effective temperature in comparison to clusters with well-determined age are shown in Figure 4(a). The effective temperatures were obtained from the TIC-v8 catalog (Stassun et al. 2019). While some of the candidates have rotation periods consistent with being young (dark gray crosses), many do not (light gray crosses). A full vetting of candidates would be required to use them to further refine the age of TOI-1268. From the rotation period only, TOI-1268's age is most likely to be between the 120 Myr Pleiades (colored in blue) and the 2.5 Gyr NGC 6819 (colored in purple).

For K-type stars like TOI-1268, lithium is expected to be depleted when the star is older than Praesepe/Hyades ages (e.g., Boesgaard et al. 2016; Cummings et al. 2017). However, Li I 6707.8 nm is clearly detected in both the TRES and NEID spectra. The equivalent width (EW) is measured to be 0.069 ± 0.011 Å from the TRES data. In Figure 2(b), we compare the Li abundance of TOI-1268 to Pleiades (120 Myr), Group X (250 Myr; Netwon et al. 2022, in preparation), and Praesepe (670 Myr) clusters. The Li measurements for Pleiades and Praseape are obtained from Zhou et al. (2021), where the spectra were obtained as part of the long-term radial-velocity surveys on the TRES spectrograph by Quinn et al. (2012) and Quinn et al. (2014). The Li abundance of TOI-1268 is richer than Praesepe and in agreement with Pleiades. Combining Li and stellar rotation period information, TOI-1268's age is likely between Pleiades and Praesepe clusters, i.e., 120–670 Myr.

We use `BAFFLES` (Stanford-Moore et al. 2020), a package that uses empirically determined relations to compute age posteriors for field stars from measurements of $\log R'_{\rm HK}$ calcium emission or lithium equivalent width absorption and $B-V$ color to estimate the age of TOI-1268. From the TRES spectra, we measure $\log R'_{\rm HK} = -4.3 \pm 0.19$. Since the $B-V$ color from the catalog has relatively large error bars, we use MIST isochrones and the best-fitted SED of TOI-1268 to derive a more accurate $B-V$ color of 0.83 ± 0.03. The ages independently estimated from the calcium emission and lithium lines are consistent with each other. The calcium age posterior gives 130 Myr–1.4 Gyr in the 1σ credible interval (CI). The lithium age posterior gives 220–500 Myr in the 1σ CI. The combined posterior estimates the age of TOI-1268 is 190–370 Myr in the 1σ CI (or 76–600 Myr in the 2σ CI).

Using the above information, we conclude that the rotation, lithium abundance, and activity index all give consistent ages, and confirm the youth of TOI-1268.

4. Planetary Properties

4.1. Transit Model

We use a quadratic limb-darkening transit model (Mandel & Agol 2002; Kipping 2013) plus a rotational Gaussian Process kernel (Foreman-Mackey et al. 2017; Foreman-Mackey 2018) to model the transit light curves and the rotational modulation introduced by stellar activity. We perform the light-curve fit using the TESS 2 minute cadence data only and also the TESS data jointly with two ground-based transits described in Section 2.2. To reduce the computational time, we trim the TESS light curves to roughly 3 times the transit duration before the ingress and after the egress. No transit-timing variations on TOI-1268b are detected in a preliminary light-curve fit. Because of that, we directly model the orbital period P and the reference mid-transit time T_C. Free parameters in our model include $\{\rho_{\rm circ}, b, r_{\rm p}/r_\star, P, T_C\}$, the quadratic limb-darkening

[50] https://github.com/adamkraus/Comove

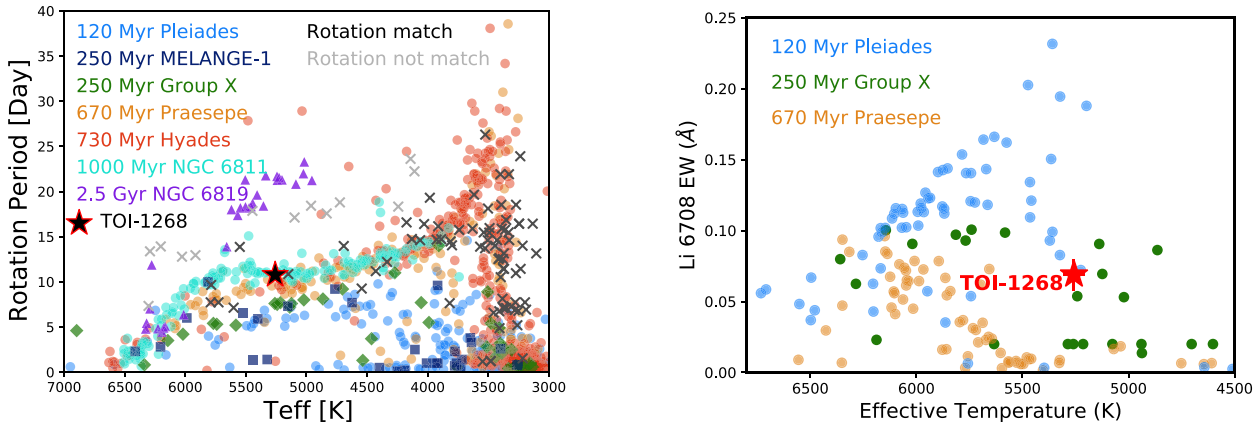

(a) Rotation period vs. effective temperature

(b) Lithium Equivalent Width (EW) vs. effective temperature

Figure 4. (a) Rotation period versus effective temperature of TOI-1268 (black star with red edge) and its neighboring stars in comparison with clusters groups with well-determined ages. The clusters we used are 120 Myr Pleiades (blue circles, Rebull et al. 2016), 250 Myr MELANGE-1 (blue squares, Tofflemire et al. 2021), 250 Myr Group X (green diamonds, E. Newton et al. 2022, in preparation), 670 Myr Praesepe and 730 Myr Hyades (orange and red circles, Douglas et al. 2016, 2019), 1 Gyr NGC 6811 (cyan circles, Curtis et al. 2019), and 2.5 Gyr NGC 6819 (purple triangles, Meibom et al. 2015). For stars we identified with the `Comove` package, the ones with rotation period and effective temperature consistent with TOI-1268 are plotted with dark gray crosses, while the ones that deviate from it are plotted with light gray crosses. (b) Lithium equivalent width (EW) vs. effective temperature of TOI-1268 (red star) and its neighboring stars in comparison with clusters groups with well-determined ages. The clusters we used are 120 Myr Pleiades (blue circles), 250 Myr Group X (green circles, E. Newton et al. 2022, in preparation), and 670 Myr Praesepe (orange circles).

parameter $\{u_0, u_1\}$, and GP parameters for the rotational kernel (see Section 3). We take the GP parameters derived from the out-of-transit TESS data as priors. Here we model $\rho_{\rm circ}$, the stellar density of the host star assuming zero eccentricity, and later compare it to the $\rho_\star$ from isochrone fitting to infer the planet's eccentricity e and argument of periapse ω. To jointly model the TESS and ground-based light curves, we use an independent pair of limb-darkening parameters for each filter and separate GP models for TESS and ground-based transits due to different cadences.

In Figure 1, we present the detrended TESS and ground-based transit light curves from a joint fit. The orbital period and transit ephemeris of the planet are tightly constrained. A summary of planetary parameters can be found in Table 1.

4.2. Stellar Obliquity Measurement

We use the NEID RM-effect signals to infer the stellar obliquity from two separate approaches: (1) model the RV anomalies reduced by the `NEID-DRP v1.1.2` and the `SERVAL` pipelines (see Section 2.6 for the description of the pipelines), and (2) directly model the planetary shadow extracted from the spectra using the planet's transit (i.e., DT; Collier Cameron et al. 2010). For both approaches, we jointly model the RM-effect signals with the TESS transit light curves. Doing so allows one to solve the complex covariances between the impact parameter b, the projected stellar obliquity λ, and the projected stellar rotation velocity $v \sin i_\star$.

For the RV fits, our model includes parameters mentioned in the transit model (Section 4.1), and also the λ, $v \sin i_\star$, and an RV jitter term $\sigma_{\rm RV}$ as free parameters. We place uniform priors on these parameters.[51] The RV anomaly due to the transit is modeled using the `starry` package (Luger et al. 2019), which takes the analytical expression of the radial velocity of a stellar disk (Short et al. 2018) and converts the polynomials to spherical harmonic coefficients. The calculated RVs do not account for macroturbulence or instrumental broadening. We incorporate `starry` into `exoplanet`, and build and sample the joint model using the `PyMC`. We also add a quadratic trend to model the baseline RV trend introduced by either the planet's orbit or stellar activity. In total, we sample four chains, each with 20,000 tuning steps and 5000 draws. A target acceptance rate of 0.95 was used. All four chains are confirmed to be converged and the inferred parameters have $\hat{R} \leqslant 1.001$. The quadratic coefficients are consistent with zeros.

For the DT fit, similar to the RV fits, we incorporate the DT data into `exoplanet`, and build and sample the joint model using the `PyMC`. At each observing time t, we calculate the planet's position on the stellar disk, assuming the star rotates as a rigid body, and identify the stellar velocity channels being blocked by the planet, v_t. To model the planetary shadow, we use a Gaussian distribution that centers at v_t and has a standard deviation of $\sqrt{v_{\rm res}^2 + v_{\rm macro}^2}$, where $v_{\rm res}$ is the velocity resolution set by the spectrograph resolution and $v_{\rm macro}$ is the macro-turbulence velocity determined by the host star. The planetary shadow is further scaled with the photometric flux at time t and normalized by the total stellar velocity flux over the planetary velocity flux. We sum up the likelihoods of the DT signals at all observing times, and infer the planet's orbital orientation, along with its TESS transit light curves. The `PyMC` setup and the convergence test are the same as the ones described in the RV fits.

In Figures 5(a) and (b), we present the NEID RVs reduced by the `NEID-DRP v1.1.2` and `SERVAL` pipelines, and their corresponding RM-effect models and uncertainties. In Figure 5(c), we show the DT data (left panel), the best-fit model (middle panel), and the residual of the data after subtracting the model (right). In all three inference models, the projected stellar obliquity $|\lambda|$ posteriors extend from 0° to 60° (3σ CIs). A polar or retrograde solution of TOI-1268 system can be ruled out. However, the differences in $|\lambda|$ posteriors

[51] We also tested placing a prior on $v \sin i_\star$ based on the observed line broadening, and found minimal changes on posteriors.

Table 1
Median Values and 68% Credible Intervals for the Stellar and Planetary Parameters of the TOI-1268 (TIC-142394656) System

Parameter	Units	Values		
Stellar Parameters				
M_*…	Mass ($M\odot$)…	0.90 ± 0.13		
R_*…	Radius ($R\odot$)…	0.86 ± 0.02		
ρ_*…	Density (cgs)…	1.98 ± 0.33		
$\log g$…	Surface gravity (cgs)…	4.52 ± 0.07		
$T_{\rm eff}$…	Effective temperature (K)…	5257 ± 40		
[M/H]…	Bulk metallicity (dex)…	$+0.17 \pm 0.06$		
$P_{\rm rot}$…	Stellar rotation period (day)…	10.84 ± 0.07		
$v_{\rm rot}$…	Equatorial velocity (km s^{-1})…	4.02 ± 0.10		
G…	Gaia G magnitude (EDR3; Lindegren et al. 2021)…	10.690 ± 0.001		
$B_{\rm P}$…	Gaia $B_{\rm P}$ magnitude (EDR3; Lindegren et al. 2021)…	11.131 ± 0.002		
$R_{\rm P}$…	Gaia $R_{\rm P}$ magnitude (EDR3; Lindegren et al. 2021)…	10.089 ± 0.001		
J…	2MASS J magnitude (Skrutskie et al. 2006)…	9.40 ± 0.02		
H…	2MASS H magnitude (Skrutskie et al. 2006)…	9.034 ± 0.023		
$K_{\rm S}$…	2MASS $K_{\rm S}$ magnitude (Skrutskie et al. 2006)…	8.911 ± 0.014		
WISE1…	WISE1 magnitude (Wright et al. 2010)…	8.886 ± 0.023		
WISE2…	WISE2 magnitude (Wright et al. 2010)…	8.941 ± 0.019		
WISE3…	WISE3 magnitude (Wright et al. 2010)…	8.846 ± 0.026		
WISE4…	WISE4 magnitude (Wright et al. 2010)…	8.878 ± 0.411		
Planetary Parameters (transit+RM-effect joint model)				
P…	Period (days)…	$8.157728^{+0.000005}_{-0.000005}$		
T_C…	Mid-transit time (BJD)…	$2{,}458{,}703.5895^{+0.0003}_{-0.0002}$		
$R_p/R_\star$ …	Planet–star radius ratio …	$0.089^{+0.001}_{-0.001}$		
R_p…	Radius (RJup) …	$0.747^{+0.018}_{-0.018}$		
		With NEID-DRP RVs	With SERVAL RVs	With DT
$\rho_{\rm circ}$	Stellar density assuming the planet has a circular orbit (cgs)…	$1.437^{+0.051}_{-0.099}$	$1.407^{+0.064}_{-0.094}$	$1.450^{+0.033}_{-0.049}$
$a/R_\star$…	Planet–star separation…	$17.164^{+0.199}_{-0.403}$	$17.043^{+0.256}_{-0.387}$	$17.215^{+0.131}_{-0.196}$
a…	Semimajor axis (au)…	$0.0684^{+0.0019}_{-0.0021}$	$0.0680^{+0.0020}_{-0.0021}$	$0.0688^{+0.0017}_{-0.0018}$
b…	Transit impact parameter …	$0.191^{+0.149}_{-0.130}$	$0.246^{+0.121}_{-0.128}$	$0.135^{+0.065}_{-0.049}$
i…	Inclination (°)…	$89.469^{+0.361}_{-0.413}$	$89.318^{+0.354}_{-0.337}$	$89.552^{+0.165}_{-0.222}$
$\lvert\lambda\rvert$…	Projected stellar obliquity (°)…	$13.623^{+14.145}_{-9.572}$	$24.873^{+12.963}_{-13.134}$	$39.997^{+7.223}_{-9.904}$
$v \sin i_\star$…	Rotational line broadening (km s^{-1})…	$4.472^{+0.454}_{-0.392}$	$4.303^{+0.553}_{-0.454}$	$4.183^{+0.306}_{-0.231}$
e…	Eccentricity…	$0.13^{+0.24}_{-0.13}$	$0.13^{+0.27}_{-0.13}$	$0.12^{+0.24}_{-0.12}$
ω…	Argument of periapse (°)…	210^{+25}_{-19}, 329^{+21}_{-25}	212^{+25}_{-20}, 328^{+19}_{-26}	210^{+24}_{-19}, 329^{+20}_{-27}
$\sigma_{\rm RV}$…	Radial-velocity jitter (m s^{-1})…	$3.473^{+1.791}_{-2.243}$	$2.255^{+1.861}_{-1.683}$	…
$v_{\rm macro}$…	Macroturbulence of the host star (km s^{-1})…	…	…	$2.020^{+0.134}_{-0.131}$
$u_{0,TESS}$…	Quadratic limb-darkening coefficient 0…	$0.235^{+0.072}_{-0.074}$	$0.236^{+0.076}_{-0.077}$	$0.239^{+0.071}_{-0.074}$
$u_{1,TESS}$…	Quadratic limb-darkening coefficient 1…	$0.473^{+0.150}_{-0.142}$	$0.462^{+0.154}_{-0.146}$	$0.478^{+0.151}_{-0.137}$

Note. Due to the asymmetric and bimodal shapes of the eccentricity and argument of periapse posteriors, instead of reporting their medians and 68% credible intervals, we report their 68% highest posterior density intervals.

from three models are still noticeable. In Table 1, we summarize the fitting parameters. The NEID-DRP RVs suggest an aligned system with $|\lambda| = 14^{+14}_{-10}$°, whereas the SERVAL RVs and DT data suggest a slightly misaligned system (i.e., $|\lambda| = 25^{+13}_{-13}$° for SERVAL and $|\lambda_{\rm DT}| = 40^{+7}_{-10}$° for DT). A possible explanation for the high stellar obliquity inferred by the DT model is the stellar obliquity and impact parameter degeneracy: low impact parameters ($b \sim 0.1$) correlate to high stellar obliquities ($\lambda \sim 40°$), and slightly higher impact parameters ($b \sim 0.2$) correlate to lower stellar obliquities ($\lambda \sim 20°$). Since a low impact parameter solution is suggested by the DT model ($b = 0.135 + 0.065 - 0.049$), we derive the high stellar obliquity solution. The DT inferred impact parameter is still consistent with the one from transit-only fit ($b = 0.2 \pm 0.1$). Breaking the degeneracy between the impact parameter and stellar obliquity will be the key step toward precise stellar obliquity measurement in future observations.

Finally, we use the inclination of the host star ($i_\star = 76° \pm 10°$) and the projected stellar obliquity to estimate the true stellar obliquity ψ of TOI-1268. Using the spherical law of cosines, $\cos\psi = \cos|\lambda| \sin i \sin i_\star + \cos i \cos i_\star$, where i is the orbital inclination, we get $\psi = 22.^\circ7 \pm 10.^\circ5$ for NEID-DRP RVs, $\psi = 30.^\circ4 \pm 11.^\circ1$ for SERVAL RVs, and $\psi = 40° \pm 10°$ for the DT signal.

5. Results and Discussion

TOI-1268 is an early K-type dwarf hosting an 8.2 day, Saturn-sized planet. Using the host star's rotation period and lithium abundance, we estimated the age of TOI-1268 between the 120 Myr Pleiades and the 670 Myr Praesepe or 730 Myr Hyades. TOI-1268b was discovered during the TESS prime mission, and validated by seeing-limited photometry, reconnaissance spectroscopy on TRES, and high-resolution imaging on `Alopeke, PHARO, Speckle Polarimeter on SAI 2.5 m, and

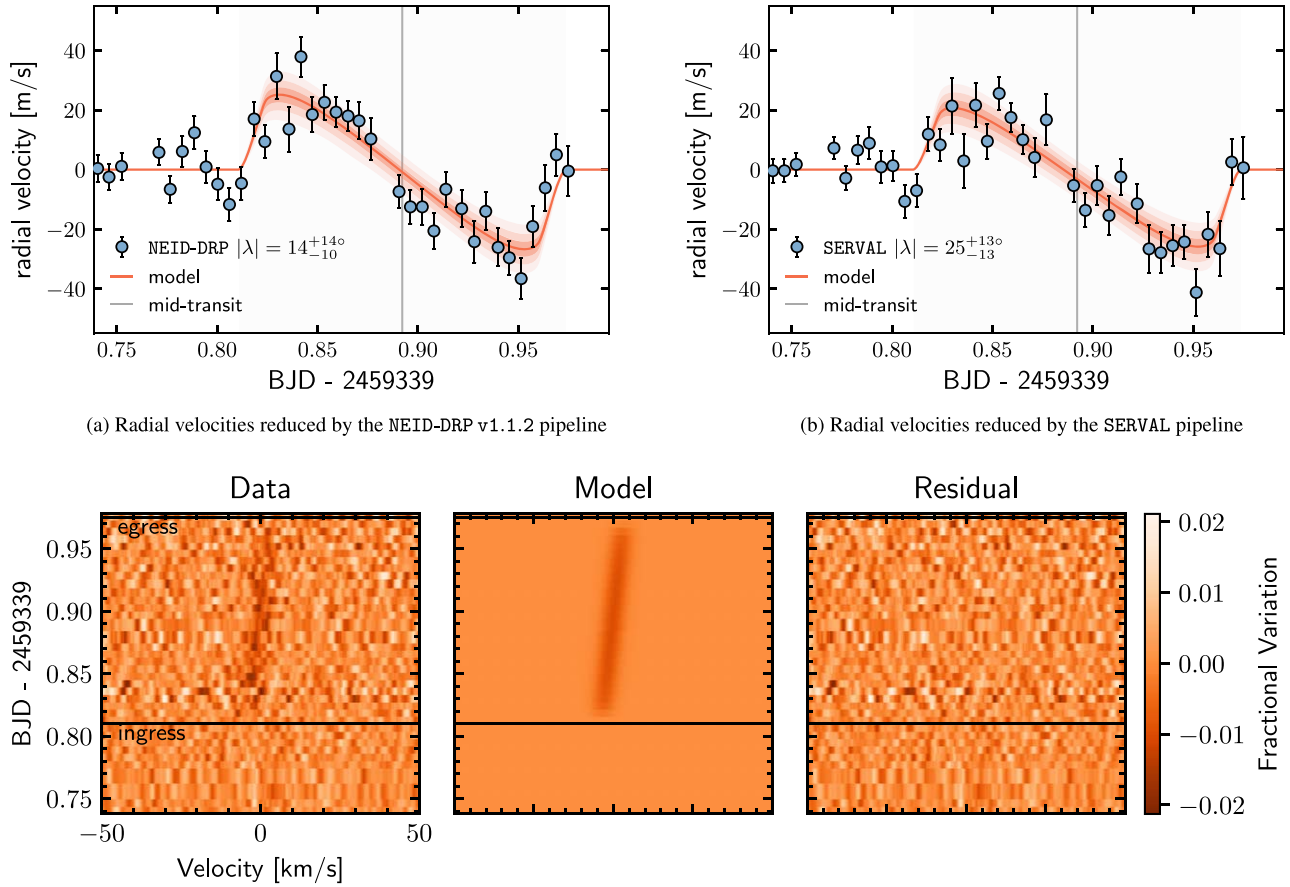

(a) Radial velocities reduced by the NEID-DRP v1.1.2 pipeline

(b) Radial velocities reduced by the SERVAL pipeline

(c) Doppler Tomography signals, from which we infer $|\lambda| = 40^{+7}_{-10}$°

Figure 5. (a) and (b) In-transit radial-velocity measurements of the TOI-1268 system using the NEID spectra. The blue dots and black bars are NEID RVs and their corresponding uncertainties. Using the RM effect, the projected stellar obliquity is constrained. (c) The Doppler tomography signal of the TOI-1268 system during TOI-1268b's transit. The left, middle, and right panels are data extracted from the NEID spectra, best-fit model, and the residual of the data after subtracting the best-fit model. The color scale presents the flux variation of the velocity channel. We expect to observe a decrease in flux in the velocity channel of the star blocked by the planet.

ShARCS. We confirmed the planet using the newly commissioned NEID spectrograph via the RM effect. The planetary nature of TOI-1268b has also been independently confirmed by the KESPRINT consortium through high-precision RV follow-up observations (Šubjak et al. 2022).

Using the NEID spectra, the stellar obliquity of TOI-1268 was constrained. The stellar obliquity and impact parameter degeneracy and the small $v \sin i_\star$ of TOI-1268 make it challenging to measure the stellar obliquity precisely from a single transit observation. However, a stellar obliquity greater than 60° can be ruled out at the 3σ level. The stellar obliquity of TOI-1268 is either aligned, suggested by the NEID-DRP RVs, or slightly misaligned, suggested by the SERVAL RVs and the DT signal. Further transit spectroscopy observations of the system will be required to resolve the minor discrepancy between the models and refine the stellar obliquity measurement. Oshagh et al. (2018) discussed how starspots could compromise stellar obliquity measurements, which further motivate multiple RM-effect measurements on young TOI-1268. TOI-1268 is one of the few studies constraining the stellar obliquity using multiple techniques (see also Knudstrup & Albrecht 2021), and one of the first studies modeling DT signals on a spotty young star with a high-precision stabilized spectrograph. Previous works have made use of lower-precision spectrographs that make such a comparison impossible.

The eccentricity of TOI-1268b inferred purely from the transit light curves and the stellar density is consistent with a circular or low-eccentricity orbit planet. Given TOI-1268b's large orbital distance ($a_p = 0.068 \pm 0.02$ au), it will require high tidal dissipation efficiency and/or a nearby companion still coupled and driving eccentricity oscillations of TOI-1268b, if the planet has undergone or is undergoing high-eccentricity tidal migration. TOI-1268b is likely an outcome of disk migration or in situ formation. The large planet–star separation ($a/R_\star \sim 17$), along with the system's young age, makes it unlikely to align with its host star by planet–star tidal interactions. The stellar obliquity of the system probes the primordial spin–orbit angles for warm Jupiters formed in situ or via disk migration and points to an aligned or slightly misaligned system. Strong primordial misalignment, such as by chaotic accretion (Bate et al. 2010), magnetic warping (Lai et al. 2011), or an inclined stellar/planetary companion (Batygin 2012), probably did not occur in the system.

In Figure 6, we present the projected stellar obliquity versus stellar age for all hot/warm Jupiters for which obliquity measurements are available (data from S. Albrecht et al. 2022, in preparation). Planets are colored by their plane–star separations ($a/R_\star$) and circles (triangles) indicate host star temperatures above (below) the Kraft break (6250 K). TOI-1268b stands out for its young age and large planet–star

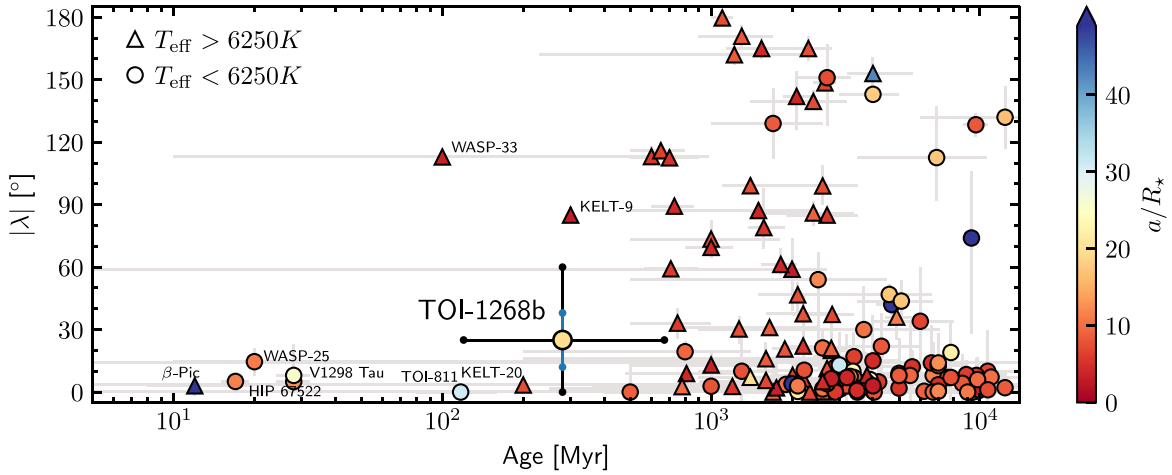

Figure 6. Projected stellar obliquity vs. estimated stellar age for all hot/warm Jupiters. Planets are colored by $a/R_\star$ and labeled in triangles or circles given their host star effective temperatures (i.e., triangles for host stars above the Kraft break $T_{\rm eff} > 6250K$ and circles for stars below the Kraft break). Gray lines show 1σ uncertainties. For TOI-1268, we plot its estimated age between the 120 Myr Pleiades and 670 Myr Praesepe clusters and its stellar obliquity using representative values inferred from SERVAL RVs labeled in blue error bars. The 3σ credible interval of obliquity posteriors derived from the RV and DT signals are shown in black.

separation. Currently, giant planets in systems younger than 100 Myr—β-Pic b (Hirano et al. 2020), WASP-25b (Brown et al. 2012), HIP 67522b (Heitzmann et al. 2021), and V1298 Tau b and c (Feinstein et al. 2021; Johnson et al. 2021)—are all found in aligned systems. TOI-1268b might lie in the transitional region where more misaligned systems get discovered. More stellar obliquity measurements of young systems are encouraged before interpreting the observations theoretically.

Computations for this research were performed on the Pennsylvania State University's Institute for Computational & Data Sciences Advanced CyberInfrastructure (ICS-ACI). This content is solely the responsibility of the authors and does not necessarily represent the views of the Institute for CyberScience. The Center for Exoplanets and Habitable Worlds is supported by the Pennsylvania State University and the Eberly College of Science. We gratefully acknowledge support by NASA XRP 80NSSC18K0355 and NASA TESS GO 80NSSC18K1695.

These results are based on observations obtained with NEID on the WIYN 3.5 m Telescope at Kitt Peak National Observatory. WIYN is a joint facility of the University of Wisconsin–Madison, Indiana University, NSF's NOIRLab, the Pennsylvania State University, Purdue University, University of California, Irvine, and the University of Missouri. The authors are honored to be permitted to conduct astronomical research on Iolkam Du'ag (Kitt Peak), a mountain with particular significance to the Tohono O'odham.

This work makes use of observations from the LCOGT network.

This work was performed for the Jet Propulsion Laboratory, California Institute of Technology, sponsored by the United States Government under the Prime Contract 80NM0018D0004 between Caltech and NASA.

The research leading to these results has received funding from the ARC grant for Concerted Research Actions, financed by the Wallonia-Brussels Federation.

TRAPPIST is funded by the Belgian Fund for Scientific Research (Fond National de la Recherche Scientifique, FNRS) under the grant PDR T.0120.21, with the participation of the Swiss National Science Foundation (SNF). TRAPPIST-North is a project funded by the University of Liege (Belgium), in collaboration with Cadi Ayyad University of Marrakech (Morocco). M.G. and E.J. are F.R.S.-FNRS Senior Research Associates.

C.D.D. acknowledges support from the NASA Exoplanet Research Program (XRP) under award 80NSSC20K0250.

A.A.B. and I.A.S. acknowledge the support of Ministry of Science and Higher Education of the Russian Federation under the grant 075-15-2020-780 (N13.1902.21.0039).

We acknowledge the use of public TESS data from pipelines at the TESS Science Office and at the TESS Science Processing Operations Center.

Resources supporting this work were provided by the NASA High-End Computing (HEC) Program through the NASA Advanced Supercomputing (NAS) Division at Ames Research Center for the production of the SPOC data products.

This research made use of `exoplanet` (Foreman-Mackey et al. 2019, 2021) and its dependencies (Astropy Collaboration et al. 2013; Kipping 2013; Salvatier et al. 2016; Theano Development Team 2016; Foreman-Mackey et al. 2017; Foreman-Mackey 2018; Astropy Collaboration et al. 2018; Foreman-Mackey et al. 2019; Luger et al. 2019; Agol et al. 2020).

Some/all of the data presented in this Letter were obtained from the Mikulski Archive for Space Telescopes (MAST) at the Space Telescope Science Institute. The specific observations analyzed can be accessed via doi:10.17909/t9-nmc8-f686.

Facilities: TESS, Gaia, LCOGT, TRAPPIST-North, PHARON, `Alopeke, ShARCS, KELT, TRES, NEID, Exoplanet Archive

Software: `ArviZ` (Kumar et al. 2019), `astroARIADNE`, `AstroImageJ` (Collins et al. 2017), `astropy` (Astropy Collaboration et al. 2013, 2018), `BAFFLES` (Stanford-Moore et al. 2020), `celerite2` (Foreman-Mackey et al. 2017; Foreman-Mackey 2018), `Comove` (Tofflemire et al. 2021), `EXOFASTv2` (Eastman et al. 2013, 2019), `exoplanet` (Foreman-Mackey et al. 2021), `Jupyter` (Kluyver et al. 2016), `Matplotlib` (Hunter 2007; Droettboom et al. 2016), `NumPy` (van der Walt et al. 2011; Harris et al. 2020), `pandas` (McKinney 2010), `PyMC` (Salvatier et al. 2016), `SciPy`

(Virtanen et al. 2020), `starry` (Luger et al. 2019), `Tapir` (Jensen 2013), `VARTOOLS` (Hartman & Bakos 2016).

ORCID iDs

Jiayin Dong https://orcid.org/0000-0002-3610-6953
Chelsea X. Huang https://orcid.org/0000-0003-0918-7484
George Zhou https://orcid.org/0000-0002-4891-3517
Rebekah I. Dawson https://orcid.org/0000-0001-9677-1296
Gumundur K. Stefánsson https://orcid.org/0000-0001-7409-5688
Chad F. Bender https://orcid.org/0000-0003-4384-7220
Cullen H. Blake https://orcid.org/0000-0002-6096-1749
Eric B. Ford https://orcid.org/0000-0001-6545-639X
Samuel Halverson https://orcid.org/0000-0003-1312-9391
Shubham Kanodia https://orcid.org/0000-0001-8401-4300
Suvrath Mahadevan https://orcid.org/0000-0001-9596-7983
Michael W. McElwain https://orcid.org/0000-0003-0241-8956
Joe P. Ninan https://orcid.org/0000-0001-8720-5612
Paul Robertson https://orcid.org/0000-0003-0149-9678
Arpita Roy https://orcid.org/0000-0001-8127-5775
Christian Schwab https://orcid.org/0000-0002-0091-7105
Daniel J. Stevens https://orcid.org/0000-0002-5951-8328
Ryan C. Terrien https://orcid.org/0000-0002-4788-8858
Andrew Vanderburg https://orcid.org/0000-0001-7246-5438
Adam L. Kraus https://orcid.org/0000-0001-9811-568X
Stephanie Douglas https://orcid.org/0000-0001-7371-2832
Elisabeth Newton https://orcid.org/0000-0003-4150-841X
Rayna Rampalli https://orcid.org/0000-0001-7337-5936
Daniel M. Krolikowski https://orcid.org/0000-0001-9626-0613
Karen A. Collins https://orcid.org/0000-0001-6588-9574
Joseph E. Rodriguez https://orcid.org/0000-0001-8812-0565
Dax L. Feliz https://orcid.org/0000-0002-2457-7889
Carl Ziegler https://orcid.org/0000-0002-0619-7639
Khalid Barkaoui https://orcid.org/0000-0003-1464-9276
Francisco J. Pozuelos https://orcid.org/0000-0003-1572-7707
Emmanuel Jehin https://orcid.org/0000-0001-8923-488X
C. Michaël https://orcid.org/0000-0003-1462-7739
Zouhair Benkhaldoun https://orcid.org/0000-0001-6285-9847
Pablo Lewin https://orcid.org/0000-0003-0828-6368
Raquel Forés-Toribio https://orcid.org/0000-0002-6482-2180
Jose A. Muñoz https://orcid.org/0000-0001-9833-2959
Kim K. McLeod https://orcid.org/0000-0001-9504-1486
Ferran Grau Horta https://orcid.org/0000-0001-9927-7269
Felipe Murgas https://orcid.org/0000-0001-9087-1245
David W. Latham https://orcid.org/0000-0001-9911-7388
Samuel N. Quinn https://orcid.org/0000-0002-8964-8377
Allyson Bieryla https://orcid.org/0000-0001-6637-5401
Steve B. Howell https://orcid.org/0000-0002-2532-2853
Crystal L. Gnilka https://orcid.org/0000-0003-2519-6161
David R. Ciardi https://orcid.org/0000-0002-5741-3047
Michael B. Lund https://orcid.org/0000-0003-2527-1598
Courtney D. Dressing https://orcid.org/0000-0001-8189-0233
Steven Giacalone https://orcid.org/0000-0002-8965-3969
Arjun B. Savel https://orcid.org/0000-0002-2454-768X
Ivan A. Strakhov https://orcid.org/0000-0003-0647-6133
Alexander A. Belinski https://orcid.org/0000-0003-3469-0989
George R. Ricker https://orcid.org/0000-0003-2058-6662
S. Seager https://orcid.org/0000-0002-6892-6948
Joshua N. Winn https://orcid.org/0000-0002-4265-047X
Jon M. Jenkins https://orcid.org/0000-0002-4715-9460
Guillermo Torres https://orcid.org/0000-0002-5286-0251
Martin Paegert https://orcid.org/0000-0001-8120-7457

References

Agol, E., Luger, R., & Foreman-Mackey, D. 2020, AJ, 159, 123
Albrecht, S., Winn, J. N., Johnson, J. A., et al. 2012, ApJ, 757, 18
Astropy Collaboration, Price-Whelan, A. M., Sipőcz, B. M., et al. 2018, AJ, 156, 123
Astropy Collaboration, Robitaille, T. P., Tollerud, E. J., et al. 2013, A&A, 558, A33
Bate, M. R., Lodato, G., & Pringle, J. E. 2010, MNRAS, 401, 1505
Batygin, K. 2012, Natur, 491, 418
Boesgaard, A. M., Lum, M. G., Deliyannis, C. P., et al. 2016, ApJ, 830, 49
Brown, D. J. A., Cameron, A. C., Anderson, D. R., et al. 2012, MNRAS, 423, 1503
Brown, T. M., Baliber, N., Bianco, F. B., et al. 2013, PASP, 125, 1031
Buchhave, L. A., Bakos, G. Á., Hartman, J. D., et al. 2010, ApJ, 720, 1118
Buchhave, L. A., Bizzarro, M., Latham, D. W., et al. 2014, Natur, 509, 593
Buchhave, L. A., Latham, D. W., Johansen, A., et al. 2012, Natur, 486, 375
Castelli, F., & Kurucz, R. L. 2004, A&A, 419, 725
Collier Cameron, A., Guenther, E., Smalley, B., et al. 2010, MNRAS, 407, 507
Collins, K., Quinn, S. N., Latham, D. W., et al. 2018, AAS Meeting, 231, 439.08
Collins, K. A., Kielkopf, J. F., Stassun, K. G., & Hessman, F. V. 2017, AJ, 153, 77
Cummings, J. D., Deliyannis, C. P., Maderak, R. M., & Steinhauer, A. 2017, AJ, 153, 128
Curtis, J. L., Agüeros, M. A., Douglas, S. T., & Meibom, S. 2019, ApJ, 879, 49
Dawson, R. I., & Johnson, J. A. 2018, ARA&A, 56, 175
Donati, J. F., Semel, M., Carter, B. D., Rees, D. E., & Collier Cameron, A. 1997, MNRAS, 291, 658
Douglas, S. T., Agüeros, M. A., Covey, K. R., et al. 2016, ApJ, 822, 47
Douglas, S. T., Curtis, J. L., Agüeros, M. A., et al. 2019, ApJ, 879, 100
Droettboom, M., Hunter, J., Caswell, T. A., et al. 2016, Matplotlib: Matplotlib v1.5.1, Zenodo, doi:10.5281/zenodo.44579
Eastman, J., Gaudi, B. S., & Agol, E. 2013, PASP, 125, 83
Eastman, J. D., Rodriguez, J. E., Agol, E., et al. 2019, 09480, arXiv:1907.09480
Feinstein, A. D., Montet, B. T., Johnson, M. C., et al. 2021, AJ, 162, 213
Foreman-Mackey, D. 2018, RNAAS, 2, 31
Foreman-Mackey, D., Agol, E., Ambikasaran, S., & Angus, R. 2017, AJ, 154, 220
Foreman-Mackey, D., Czekala, I., Luger, R., et al. 2019, dfm/exoplanet: exoplanet v0.2.1, Zenodo doi:10.5281/zenodo.3462740
Foreman-Mackey, D., Luger, R., Agol, E., et al. 2021, JOSS, 6, 3285
Gagné, J., Mamajek, E. E., Malo, L., et al. 2018, ApJ, 856, 23
Gavel, D., Kupke, R., Dillon, D., et al. 2014, Proc. SPIE, 9148, 914805
Halverson, S., Terrien, R., Mahadevan, S., et al. 2016, Proc. SPIE, 9908, 99086P
Harris, C. R., Jarrod Millman, K., van der Walt, S. J., et al. 2020, Natur, 585, 357
Hartman, J. D., & Bakos, G. Á. 2016, A&C, 17, 1
Hayward, T. L., Brandl, B., Pirger, B., et al. 2001, PASP, 113, 105
Heitzmann, A., Zhou, G., Quinn, S. N., et al. 2021, ApJL, 922, L1
Hirano, T., Krishnamurthy, V., Gaidos, E., et al. 2020, ApJL, 899, L13
Hirsch, L. A., Ciardi, D. R., Howard, A. W., et al. 2019, ApJ, 878, 50
Huang, C. X., Vanderburg, A., Pál, A., et al. 2020a, RNAAS, 4, 204
Huang, C. X., Vanderburg, A., Pál, A., et al. 2020b, RNAAS, 4, 206
Hunter, J. D. 2007, CSE, 9, 90
Jenkins, J. M., Twicken, J. D., McCauliff, S., et al. 2016, Proc. SPIE, 9913, 99133E
Jensen, E. 2013, Tapir: A web interface for transit/eclipse observability, Astrophysics Source Code Library, ascl:1306.007
Johnson, M. C., David, T. J., Petigura, E. A., et al. 2021, arXiv:2110.10707
Kanodia, S., Mahadevan, S., Ramsey, L. W., et al. 2018, Proc. SPIE, 10702, 107026Q
Kipping, D. M. 2013, MNRAS, 435, 2152
Kluyver, T., Ragan-Kelley, B., Pérez, F., et al. 2016, in Positioning and Power in Academic Publishing: Players, Agents and Agendas, ed. F. Loizides & B. Scmidt (Amsterdam: IOS Press), 87
Knudstrup, E., & Albrecht, S. 2021, arXiv:2111.14968
Kumar, R., Carroll, C., Hartikainen, A., & Martin, O. 2019, JOSS, 4, 1143
Kupke, R., Gavel, D., Roskosi, C., et al. 2012, Proc. SPIE, 8447, 84473G
Lai, D., Foucart, F., & Lin, D. N. C. 2011, MNRAS, 412, 2790
Lindegren, L., Klioner, S. A., Hernández, J., et al. 2021, A&A, 649, A2
Lomb, N. R. 1976, Ap&SS, 39, 447
Luger, R., Agol, E., Foreman-Mackey, D., et al. 2019, AJ, 157, 64
Mandel, K., & Agol, E. 2002, ApJL, 580, L171

Masuda, K., & Winn, J. N. 2020, AJ, 159, 81
McKinney, W. 2010, in Proc. of the 9th Python in Science Conf., ed. S. van der Walt & J. Millman (Austin, TX: SciPy), 61
McLaughlin, D. B. 1924, ApJ, 60, 22
Meibom, S., Barnes, S. A., Platais, I., et al. 2015, Natur, 517, 589
Oshagh, M., Triaud, A. H. M. J., Burdanov, A., et al. 2018, A&A, 619, A150
Pepper, J., Gould, A., & Depoy, D. L. 2003, AcA, 53, 213
Pepper, J., Pogge, R. W., DePoy, D. L., et al. 2007, PASP, 119, 923
Petrovich, C. 2015, ApJ, 805, 75
Quinn, S. N., White, R. J., Latham, D. W., et al. 2012, ApJL, 756, L33
Quinn, S. N., White, R. J., Latham, D. W., et al. 2014, ApJ, 787, 27
Rebull, L. M., Stauffer, J. R., Bouvier, J., et al. 2016, AJ, 152, 113
Ricker, G. R., Winn, J. N., Vanderspek, R., et al. 2015, JATIS, 1, 014003
Robertson, P., Anderson, T., Stefansson, G., et al. 2019, JATIS, 5, 015003
Rogers, T. M., Lin, D. N. C., & Lau, H. H. B. 2012, ApJL, 758, L6
Rogers, T. M., Lin, D. N. C., McElwaine, J. N., & Lau, H. H. B. 2013, ApJ, 772, 21
Rossiter, R. A. 1924, ApJ, 60, 15
Salvatier, J., Wiecki, T. V., & Fonnesbeck, C. 2016, PeerJ Comput. Sci., 2, e55
Savel, A. B., Dressing, C. D., Hirsch, L. A., et al. 2020, AJ, 160, 287
Scargle, J. D. 1982, ApJ, 263, 835
Schwab, C., Rakich, A., Gong, Q., et al. 2016, Proc. SPIE, 9908, 99087H
Scott, N. J. 2019, BAAS, 51, 330.15
Short, D. R., Orosz, J. A., Windmiller, G., & Welsh, W. F. 2018, AJ, 156, 297
Skrutskie, M. F., Cutri, R. M., Stiening, R., et al. 2006, AJ, 131, 1163
Stanford-Moore, S. A., Nielsen, E. L., De Rosa, R. J., Macintosh, B., & Czekala, I. 2020, ApJ, 898, 27
Stassun, K. G., Oelkers, R. J., Paegert, M., et al. 2019, AJ, 158, 138
Stefansson, G., Hearty, F., Robertson, P., et al. 2016, ApJ, 833, 175
Stefansson, G., Mahadevan, S., Petrovich, C., et al. 2021, arXiv:2111.01295
Stumpe, M. C., Smith, J. C., Catanzarite, J. H., et al. 2014, PASP, 126, 100
Stumpe, M. C., Smith, J. C., Van Cleve, J. E., et al. 2012, PASP, 124, 985
Šubjak, J., Endl, M., Chaturvedi, P., et al. 2022, arXiv:2201.13341
Theano Development Team 2016, arXiv:1605.02688
Tofflemire, B. M., Rizzuto, A. C., Newton, E. R., et al. 2021, AJ, 161, 171
van der Walt, S., Colbert, S. C., & Varoquaux, G. 2011, CSE, 13, 22
VanderPlas, J. T. 2018, ApJS, 236, 16
Virtanen, P., Gommers, R., Oliphant, T. E., et al. 2020, NatMe, 17, 261
Winn, J. N., Fabrycky, D., Albrecht, S., & Johnson, J. A. 2010, ApJL, 718, L145
Wright, E. L., Eisenhardt, P. R. M., Mainzer, A. K., et al. 2010, AJ, 140, 1868
Zechmeister, M., Reiners, A., Amado, P. J., et al. 2018, A&A, 609, A12
Zhou, G., Quinn, S. N., Irwin, J., et al. 2021, AJ, 161, 2